

ARTICLE

<https://doi.org/10.1038/s41467-019-09210-0>

OPEN

Tuning orbital orientation endows molybdenum disulfide with exceptional alkaline hydrogen evolution capability

Yipeng Zang¹, Shuwen Niu¹, Yishang Wu¹, Xusheng Zheng², Jinyan Cai¹, Jian Ye², Yufang Xie¹, Yun Liu¹, Jianbin Zhou¹, Junfa Zhu², Xiaojing Liu¹, Gongming Wang¹ & Yitai Qian¹

Molybdenum disulfide is naturally inert for alkaline hydrogen evolution catalysis, due to its unfavorable water adsorption and dissociation feature originated from the unsuitable orbital orientation. Herein, we successfully endow molybdenum disulfide with exceptional alkaline hydrogen evolution capability by carbon-induced orbital modulation. The prepared carbon doped molybdenum disulfide displays an unprecedented overpotential of 45 mV at 10 mA cm⁻², which is substantially lower than 228 mV of the molybdenum disulfide and also represents the best alkaline hydrogen evolution catalytic activity among the ever-reported molybdenum disulfide catalysts. Fine structural analysis indicates the electronic and coordination structures of molybdenum disulfide have been significantly changed with carbon incorporation. Moreover, theoretical calculation further reveals carbon doping could create empty 2p orbitals perpendicular to the basal plane, enabling energetically favorable water adsorption and dissociation. The concept of orbital modulation could offer a unique approach for the rational design of hydrogen evolution catalysts and beyond.

¹Hefei National Laboratory for Physical Sciences at the Microscale and Department of Chemistry, University of Science & Technology of China, 230026 Hefei, Anhui, China. ²National Synchrotron Radiation Laboratory, University of Science & Technology of China, 230029 Hefei, China. These authors contributed equally: Yipeng Zang, Shuwen Niu. Correspondence and requests for materials should be addressed to X.L. (email: liuxj206@ustc.edu.cn) or to G.W. (email: wanggm@ustc.edu.cn)

Sustainable hydrogen production in an economical way is the key to building new hydrogen-based energy system¹. Water electrolysis driven by renewable energy sources such as solar, wind, or geothermal energy has been regarded as the most promising way for sustainable hydrogen production^{2,3}. Despite the fact that water electrolysis is first discovered in acidic condition, alkaline electrolysis is more preferred in industrial plants, due to the robustness of electrode materials, long lifetime, and cheap electrolyzer construction⁴. Electrocatalysts, as the heart of the electrolyzers, significantly affect the cell efficiency⁵. Unfortunately, precious platinum-based materials till now are still the state-of-the-art hydrogen evolution reaction (HER) catalysts in both acidic and alkaline conditions^{6,7}. In this regard, developing non-noble metal-based HER catalysts to replace Pt has been one of the focal points over the past decades^{8–14}.

Molybdenum disulfide (MoS₂), a typical cost-effective layered transition metal dichalcogenide^{15–18}, has been proved both theoretically and experimentally to be highly active for HER catalysis in acidic condition^{16–26}. The edged Mo and S atoms with a free energy of H adsorption close to zero are commonly believed to be the catalytic sites^{19,27–30}. Unfortunately, MoS₂ is found to be inactive in alkaline condition^{7,31,32}, while the alkaline catalysis is more practically viable. The inert alkaline electrolysis is mainly attributed to the sluggish water adsorption and dissociation dynamics, which is, in essence, determined by the intrinsic structural feature of MoS₂^{19,33–35}. As the dominated orbital compositions of the conduction band in MoS₂, both the Mo 4d_{z²} orbitals in the central sublayer and the S 3p_{x,y} orbitals in the outermost sublayers possess unfavorable charge interaction with water molecule due to the steric effect (d_{z²}) and unsuitable orbital orientation (3p_{x,y}) in the basal plane, which essentially hinder the water adsorption and dissociation on MoS₂ (Fig. 1). Although improving the conductivity of MoS₂^{31,36,37} or surface modification with water adsorption components^{19,33,34} has shown enhanced alkaline electrolysis, the overall performance of MoS₂ is still far from being satisfactory for practical alkaline electrolysis and studies on this issue are also very limited. Moreover, the understanding of the alkaline catalytic essences especially at atomic levels is also absent. Therefore, rationally tailoring the catalytic sites to endow MoS₂ with efficient alkaline HER catalytic activity is highly desirable but extremely challenging as well.

To essentially manipulate the intrinsic properties of MoS₂ for alkaline HER catalysis, tuning the orbital orientation of the MoS₂ layer to promote water adsorption and dissociation dynamics is the key. Considering carbon with smaller atomic radius and less

electrons owns more empty and lower-energy 2p valence orbitals than sulfur, partially substituting S with carbon in MoS₂ could generate sp² hybrid sites in the outermost sublayers of MoS₂, which consequently vacate one p orbital perpendicular to the basal plane for water adsorption and activation. Herein, we successfully endow MoS₂ nanosheets with exceptional alkaline HER activities by carbon-induced surface orbital orientation modulation. Carbon is in-situ incorporated into MoS₂ through a unique incomplete sulfurization of Mo₂C. The prepared carbon doped MoS₂ (C–MoS₂) nanosheets display an unprecedented overpotential of 45 mV at 10 mA cm^{−2} in alkaline condition, which represents the best alkaline HER activity among the ever-reported MoS₂-based catalysts. X-ray photoelectron spectroscopy (XPS) and X-ray absorption spectroscopy (XAS) systematically reveal the structural and electronic evolution of MoS₂ after carbon doping. Moreover, density functional theory (DFT) analysis indicates carbon doping can generate empty p orbitals perpendicular to the basal plane of MoS₂ for water adsorption and dissociation, which is essential for the alkaline HER catalysis. More importantly, the capability to endow materials with the properties which are not readily available in nature by rational orbital modulation offers a new vision for the design of HER catalysts and beyond.

Results

Synthesis and structural characterization of C–MoS₂. C–MoS₂ and MoS₂ were synthesized via a controlled sulfurization of Mo₂C, which is illustrated in Fig. 2a. Mo₂C as the precursor was obtained by a previously developed method (details, see Methods)³⁸. Then, the as-synthesized Mo₂C was controllably sulfurized to C–MoS₂ and MoS₂ in a home-built tube furnace with sulfur powder as the sulfur source and argon as the carrier gas (details, see Methods). The synthesized Mo₂C, C–MoS₂, and MoS₂ were further characterized by field-emission scanning electron microscopy (SEM), X-ray diffraction (XRD), Raman spectrum, and transmission electron microscopy (TEM), respectively. SEM images in Supplementary Fig. 1 indicate the carbon fibers of the carbon cloth (CC) substrate are uniformly coated with porous Mo₂C thin film, which becomes rougher after sulfurization treatment. XRD patterns (Fig. 2b) clearly reveal the Mo₂C (JCPDS No. 00-035-0787) can be well converted to hexagonal MoS₂ (JCPDS No. 01-073-1508) after controlled sulfurization treatment. The sharp diffraction feature of MoS₂ with deep sulfurization suggests improved crystallinity. In addition, the sulfurization process can also be revealed by Raman spectroscopy (Supplementary Fig. 2). The fingerprint bands of Mo₂C located at 662.5, 816.4, and 991.8 cm^{−1} disappear after sulfurization treatment³⁹; meanwhile, new bands centered at around 376 and 402 cm^{−1} emerge, which can be assigned to the in-plane (E_{2g}) and out-plane (A_{1g}) Mo–S phonon mode vibration of MoS₂, respectively⁴⁰. Moreover, the wavenumbers of E_{2g} and A_{1g} of C–MoS₂ display a positive shift relative to the MoS₂, probably due to the susceptibility of electron–phonon coupling induced by carbon doping^{41,42}. Taken together, all these results illustrate sulfurization treatment can well control the conversion from Mo₂C to MoS₂.

Furthermore, TEM was employed to acquire the microstructural features of Mo₂C, C–MoS₂, and MoS₂, as shown in Supplementary Fig. 3 and Fig. 2c. The high-resolution TEM (HRTEM) images exhibit well-resolved lattice fringes, where the interplanar spacing of 0.23 nm is assigned to the (101) plane of Mo₂C and 0.62 nm is assigned to the (002) plane of MoS₂, respectively. Interestingly, both C–MoS₂ and MoS₂ prepared by sulfurization treatment are composed of ultrathin layered MoS₂ nanosheets. It is also worth mentioning that no obvious carbon coating is observed on the surfaces of Mo₂C, C–MoS₂, and

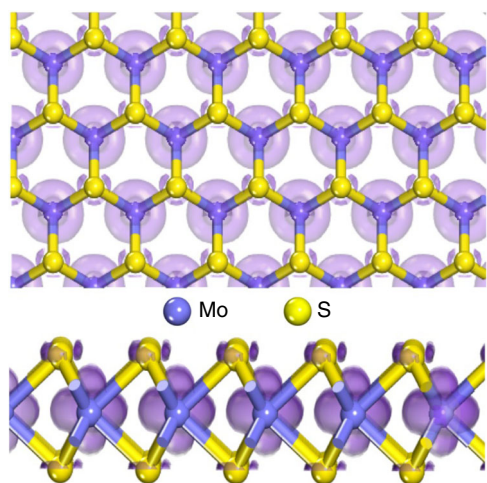


Fig. 1 The orbital analysis of the MoS₂. The top-view (upper) and side-view (lower) orbital compositions of the conduction band in MoS₂

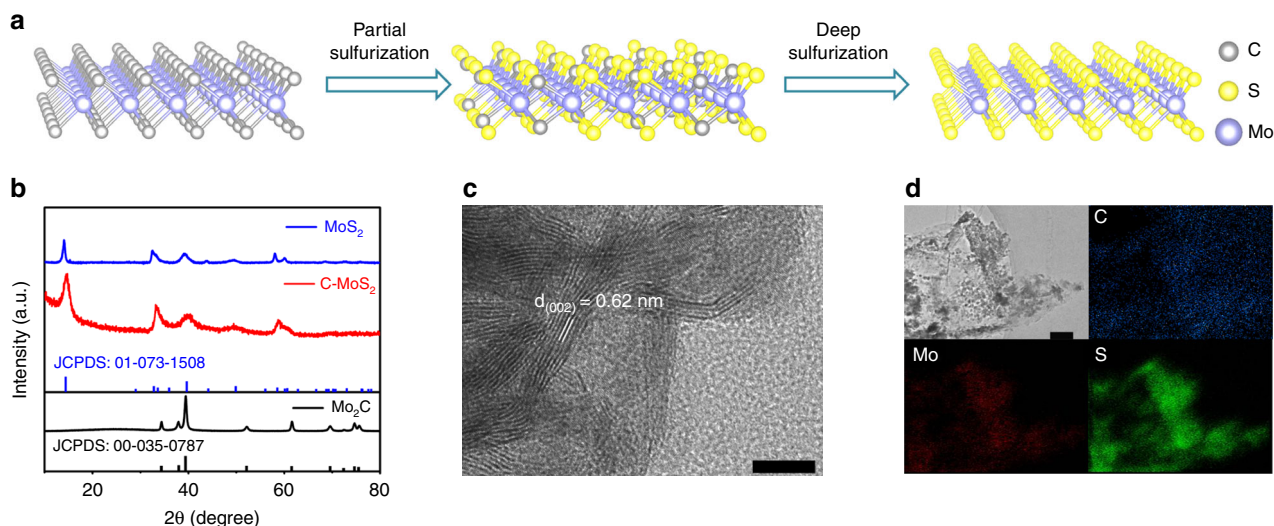


Fig. 2 Synthesis and characterization of C-MoS₂ nanosheets. **a** The schematic illustration of the synthesis of C-MoS₂ and MoS₂. **b** The XRD patterns of Mo₂C, C-MoS₂, and MoS₂. **c** The HRTEM image of C-MoS₂. The scale bar is 10 nm. **d** The TEM image and the corresponding element mapping images of C, Mo, and S elements in C-MoS₂. The scale bar is 200 nm

MoS₂ (Supplementary Fig. 2 and Fig. 2c), offering an ideal platform to probe the intrinsic effects of carbon dopants on the properties of MoS₂. In addition, the TEM image and the corresponding energy-dispersive X-ray spectroscopy (EDX) mapping images of C-MoS₂ reveal homogeneous elemental distribution of C, Mo, and S elements in C-MoS₂ (Fig. 2d), also suggesting possible carbon doping in the MoS₂.

Chemical states and coordination structures of C-MoS₂. Given that EDX spectroscopy only provides composition information that is not convincing enough to prove carbon doping into MoS₂, XPS, and XAS are further used to probe localized electronic states and coordination structures of C-MoS₂. Figure 3a shows the XPS Mo 3d spectra of Mo₂C, MoS₂, and C-MoS₂, respectively. Obviously, the typical characteristics of Mo-C bonds are observed at 231.1 and 228.0 eV in Mo₂C, while a pair of new peaks located at 232.6 and 229.5 eV appear after deep sulfurization, which can be assigned to the Mo 3d_{3/2} and Mo 3d_{5/2} of Mo-S bond in MoS₂, respectively⁴³. Strikingly, the Mo 3d profiles in C-MoS₂ exhibit obvious shoulders at the lower binding energy region, suggesting the existence of multiple chemical states of Mo. The Mo 3d spectrum of C-MoS₂ can be further deconvoluted into two pairs of peaks corresponding to the chemical states of S-Mo-S and S-Mo-C, which indicates carbon has been substitutionally doped into the MoS₂ lattices (The fitting parameters are summarized in Supplementary Table 1). Meanwhile, the C 1s spectra of C-MoS₂ and Mo₂C (Supplementary Fig. 4, the fitting parameters in Supplementary Table 2) also support the existence of Mo-C bonds in C-MoS₂. In addition, the slight shift of S 2s position suggests the chemical environments around S atoms also slightly changes after carbon doping, which could be originated from the electronegativity difference between C and S.

To probe the evolution of localized coordination environment in MoS₂ induced by carbon doping, X-ray absorption near-edge structure (XANES) and extended X-ray absorption fine structure (EXAFS) are performed. Figure 3b shows the Mo K-edge XANES spectra of Mo₂C, C-MoS₂, MoS₂, and Mo foil, in which Mo foil is used as the reference. Apparently, the Mo foil possesses the smallest energy of absorption edge. Moreover, the enlarged Mo K-edge XANES curves (inset, Fig. 3b) reveal that the near-edge absorption energy of C-MoS₂ located between MoS₂ and Mo₂C indicates the average electron density around Mo in C-MoS₂ is

higher than MoS₂ but lower than Mo₂C, which is consistent to the XPS Mo 3d spectra and also suggests the existence of Mo-C bonds in C-MoS₂. In addition, Mo K-edge extended XAFS oscillation functions $k^2\chi(k)$ of MoS₂, C-MoS₂, Mo₂C, and MoS₂ mixed with small amounts of Mo₂C (denoted as Mo₂C + MoS₂) are presented in Supplementary Fig. 5a, respectively. Clearly, the oscillation of C-MoS₂ is very similar to MoS₂, but quite different from Mo₂C and Mo₂C + MoS₂, convincingly indicating the C-MoS₂ possesses similar structure to MoS₂ and there is no obvious Mo₂C remaining in C-MoS₂. Moreover, the XPS depth profiling analysis also does not show obvious existence of Mo₂C (Supplementary Fig. 5b). Figure 3c displays the corresponding R-space curves of Mo after $k^2[\chi(k)]$ weighted Fourier transform. The shoulder peaks at around 1.9 and 2.9 Å in MoS₂ are originated from the Mo-S and Mo-Mo vectors, respectively⁴⁴. Considering the positions of Mo-C and Mo-O are very close and no obvious Mo-O states are observed in the XPS Mo 3d spectra, we reasonably believe the peak at 1.3 Å in C-MoS₂ could be assigned to the Mo-C bond⁴⁵. To more clearly reveal the coordination structures in C-MoS₂, wavelet transform (WT) with high resolution in both k and R spaces of Mo K-edge EXAFS oscillation are further performed. The whole WT contour spectra are shown in the Fig. 3d (the upper). The intensity maxima at $R = 1.9$ and 2.9 Å are attributed to the Mo-S and Mo-Mo bonds, respectively. Owing to the small bond length difference between Mo-C and Mo-S, more-refined first shell analysis of MoS₂ and C-MoS₂ is further carried out (Fig. 3d, the lower). Apparently, MoS₂ possesses only one contour centered at about $k = 5.4$ Å⁻¹, originated from the Mo-S bond, while C-MoS₂ presents one more maximum intensity at $k = 4.6$ Å⁻¹, which is very close to the Mo-C in Mo₂C centered at about $k = 4.5$ Å⁻¹ (Supplementary Fig. 6a) and far from the Mo-O in MoO₂ with the maximum intensity at $k = 6.0$ Å⁻¹ (Supplementary Fig. 6b), and thus can be well assigned to the Mo-C. Meanwhile, we also conduct the EXAFS fitting in the range of 1.1 to 2.3 Å by using the Mo-O and Mo-C path at 1.3 Å, respectively (Supplementary Fig. 6c,d). Based on the fitting parameters presented in the Supplementary Table 3, the R_f value for the Mo-O model (2.9%) is much larger than that of the Mo-C path (1.1%), further suggesting the Mo-C path is more likely than the Mo-O path in the C-MoS₂. In light of the formation of Mo-C in C-MoS₂, the coordination environment of MoS₂ may also alter with carbon doping. Furthermore, the EXAFS

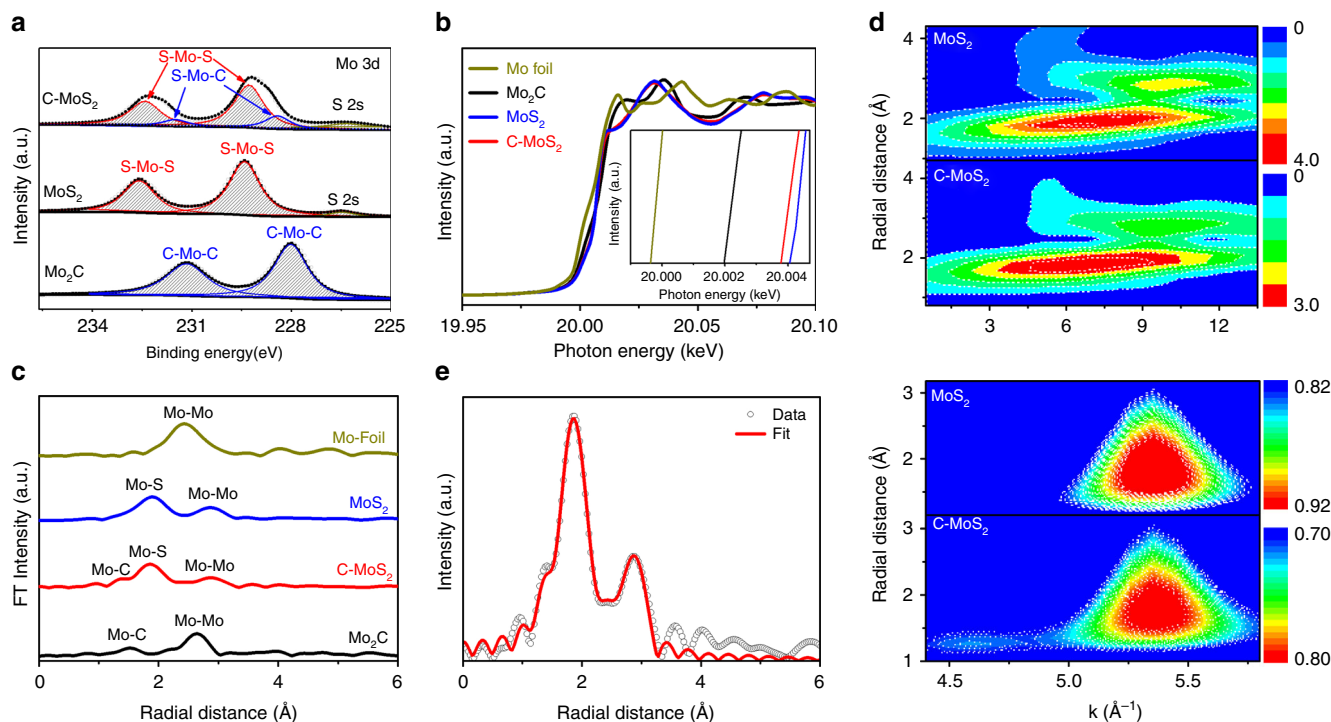


Fig. 3 Chemical states and coordination structures of C-MoS₂. **a** XPS core-level Mo 3d spectra of Mo₂C, MoS₂, and C-MoS₂, respectively. **b** The normalized Mo K-edge XANES spectra. Inset: the enlarged Mo K-edge XANES spectra. **c** Fourier transform (FT) of Mo K-edge of Mo₂C, C-MoS₂, MoS₂, and Mo foil. **d** The whole contour plots of wavelet transform (WT) of MoS₂ and C-MoS₂ (upper) and the more-refined first shell analysis (lower). **e** Radial distribution of Fourier-transformed EXAFS signal of C-MoS₂

data of MoS₂ and C-MoS₂ are fitted through the Artemis to get detailed structural parameters (Supplementary Fig. 7 and Fig. 3e). The coordination number of Mo-S is fitted to be around 6 for the MoS₂, while the coordination number of Mo-S is decreased to 4.8 and the coordination number of Mo-C is 1.1 in the C-MoS₂. The detailed fitting parameters are summarized in Supplementary Table 4. Although we cannot exclude the existence of Mo₂C clusters in C-MoS₂ that is beyond the detection limits of the currently used characterization techniques, our experimental results clearly reveal that carbon is most probably doped into the lattices of MoS₂ in the form of Mo-C bond.

Alkaline hydrogen evolution catalysis of C-MoS₂. The alkaline HER catalysis is evaluated in 1.0 M KOH solution using a typical three-electrode system with the studied materials as the working electrodes, Hg/HgO as the reference electrode and graphite rod as the counter electrode. Figure 4a shows the linear sweep voltammetry (LSV) curves of CC, Mo₂C, C-MoS₂, MoS₂, and Pt/C with a scan rate of 5 mV s⁻¹, in which the blank CC and benchmark Pt/C are used as control samples. Impressively, C-MoS₂ delivers higher current density and lower current onset potential than CC, MoS₂, and Mo₂C, indicating carbon doping can substantially improve the catalytic performance toward HER in alkaline condition. Carbon doping enables the overpotential of C-MoS₂ at 10 mA cm⁻² to be as low as 45 mV, which is much better than the 200 mV of Mo₂C and 228 mV of MoS₂ and even close to the catalytic activity of Pt/C (30 mV). Although the performance of C-MoS₂ is not the best among all kinds of the HER catalysts including non-precious and precious catalysts, C-MoS₂ represents the best alkaline HER activity among the ever-reported MoS₂ (Fig. 4b and Supplementary Table 5 and 6)^{7,19,32–34,36,37,46–48}, which could provide valuable insights for the active site engineering. The faradaic efficiency of the

C-MoS₂ for HER catalysis is estimated to be around 97%. Given that temperature can well control the sulfurization degrees, we also study the sulfurization degree-dependent HER activities (Supplementary Fig. 8). With the increase of the sulfurization temperatures, the HER overpotentials display an inverse volcano-shaped feature. At the temperature below 500 °C, Mo₂C cannot be completely converted to MoS₂ and the corresponding catalytic activity is far less than that of the C-MoS₂, further revealing C doping probably plays vital role in the HER catalysis. To probe the effects of carbon contents, we further study the carbon content dependent HER activities of C-MoS₂ (Supplementary Fig. 9). Obviously, with the increase of carbon concentration, the catalytic activity of C-MoS₂ increases and reaches a maximum value. However, further increasing the C ratio will result in performance decay probably due to too much destroy of the layered structures of MoS₂, suggesting moderate carbon doping in MoS₂ is essential for the HER catalysis. Additionally, Tafel slope can be used to probe the effects of carbon dopants on the rate-determining steps during HER process. Figure 4c displays the corresponding Tafel curves. The derived Tafel slope of MoS₂ is around 129 mV dec⁻¹, suggesting the alkaline HER catalysis on MoS₂ undergoes Volmer mechanism and water dissociation is the rate-determining step. Importantly, C-MoS₂ exhibits a substantially decreased Tafel slope of 46 mV dec⁻¹, clearly revealing the sluggish water dissociation behavior has been significantly improved after carbon doping. Meanwhile, the exchange current densities for Mo₂C, MoS₂, C-MoS₂, and Pt/C derived by Tafel extrapolation are 0.12, 0.25, 0.87, and 1.28 mA cm⁻², respectively. Clearly, although the exchange current density of C-MoS₂ is a little smaller than that of Pt, it is still substantially larger than that of MoS₂, also suggesting carbon doping can change the intrinsic catalytic activities of MoS₂ for alkaline HER catalysis.

Considering surface area may also affect the HER catalytic performance, we further estimate the electrochemical surface

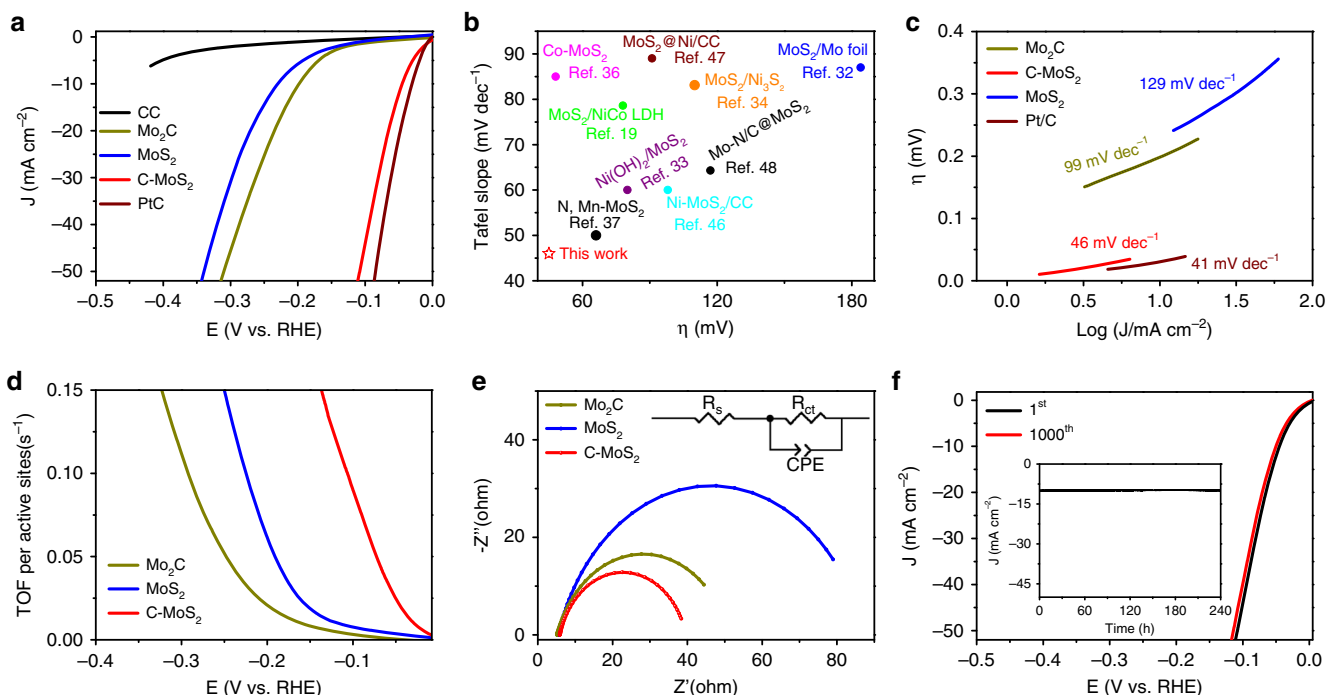


Fig. 4 Alkaline HER catalysis of C-MoS₂. **a** The LSV curves of CC, Mo₂C, C-MoS₂, MoS₂, and Pt/C with IR correction. **b** Performance comparison of C-MoS₂ with the ever-reported MoS₂-based catalysts in alkaline condition. **c** The corresponding Tafel slopes. **d** The potential-dependent TOF curves of Mo₂C, MoS₂, and C-MoS₂. **e** Nyquist plots of Mo₂C, MoS₂, and C-MoS₂ collected at the potential of 100 mV vs. RHE. **f** The initial and 1000th polarization curves of C-MoS₂. The inset is the chronoamperometric curve recorded at -0.1 V vs. RHE without IR correction for a continuous 240 h

areas of the studied materials by deriving the electrochemical double layer capacitance (C_{dl}) from the cyclic voltammetry studies (Supplementary Fig. 10)¹¹. The C-MoS₂ is found to have a larger C_{dl} of 54 mF cm⁻² than MoS₂ (19 mF cm⁻²) and Mo₂C (27 mF cm⁻²), indicating carbon doping treatment can also increase the surface area of C-MoS₂. To eliminate the influence of surface area and reveal the intrinsic catalytic behavior, turnover frequency (TOF), a surface area independent figure of merit, is calculated to gain the intrinsic per-site activity, as shown in Fig. 4d. Impressively, the TOF values of C-MoS₂ are significantly larger than those of MoS₂ and Mo₂C, clearly revealing carbon doping can essentially promote the per-site activity for HER catalysis. Additionally, electrochemical impedance spectroscopy (EIS) in Fig. 4e presents that C-MoS₂ possesses a smaller charge transfer resistance (R_{ct}) of 32.1 Ω than MoS₂ (83.7 Ω) and Mo₂C (59.7 Ω), further suggesting carbon doping in MoS₂ can also substantially boost the interfacial electron-transfer kinetics. Besides carbon doping, the superior electrochemical behavior of C-MoS₂ is also attributed to the unique carbon doping strategy without involving carbon deposition on the catalyst surface. We also use a conventional post-doping method to introduce carbon and study their electrochemical performance, shown in Supplementary Fig. 11. TEM image clearly illustrates obvious carbon shell deposited on the surface of MoS₂, which results in decreased catalytic performance probably due to the blocked active sites for catalysis (Supplementary Fig. 12). Given that the MoS₂ is derived from Mo₂C which may have tiny amounts of carbon remaining, MoS₂ with minimum carbon interference is also prepared by thermal sulfurization of ammonium molybdate (Supplementary Fig. 13). Electrochemical studies reveal that the HER performance of the newly prepared MoS₂ is far less than that of C-MoS₂, also suggesting carbon dopants play vital roles in the HER catalysis of C-MoS₂. Finally, the stability of C-MoS₂ is evaluated by polarization cycling and chronoamperometric test, both of which display superior catalytic stability for alkaline electrolysis (Fig. 4f).

XPS and XAFS are further employed to evaluate the C-MoS₂ after the stability test (Supplementary Fig. 14). Impressively, there is no big difference in chemical and bonding states in C-MoS₂ before and after the durability test, suggesting the robustness of the C-MoS₂ for HER catalysis.

Discussion

To decipher the modulation essence of the carbon dopants in C-MoS₂ for alkaline HER catalysis at the atomic level, DFT calculations are further carried out. The C content used in the C-MoS₂ model is based on the area ratio of Mo-C and Mo-S states in the XPS Mo 3d of C-MoS₂. In light of the charge balance after carbon doping, we also introduce sulfur vacancies (V_s) in the structural models. To equally distribute the positions of the C dopants and S vacancies, we considered seven different configurations, as shown in Supplementary Fig. 15. Supplementary Fig. 16 shows one of the typical structures of C-MoS₂, where the C dopants are pulled into the sublayer of MoS₂, due to the formed stronger Mo-C bond with shorter bond length than the original Mo-S bond. Detailed bond length information is provided in Supplementary Fig. 17. The electron density difference images in Supplementary Figs 18 and 19 clearly reveal that the introduction of carbon can significantly break the unified surface electron distribution of MoS₂. More importantly, the orbital analysis in Fig. 5a and b indicates the carbon dopants prefer to form the sp² hybrid orbitals (highlighted by red dash circle in Fig. 5a), which thus vacates an unhybridized 2p_z orbital perpendicular to the basal plane (highlighted by red dash circle in Fig. 5b). This 2p_z orbital orientation can maximize the head-on orbital overlapping to form sigma bonds, which can potentially offer active sites for water adsorption and activation. This orbital orientation is also consistently observed on the other structural configurations of C-MoS₂, as shown in Supplementary Fig. 15. Additionally, the detailed partial density of states (PDOS) analysis

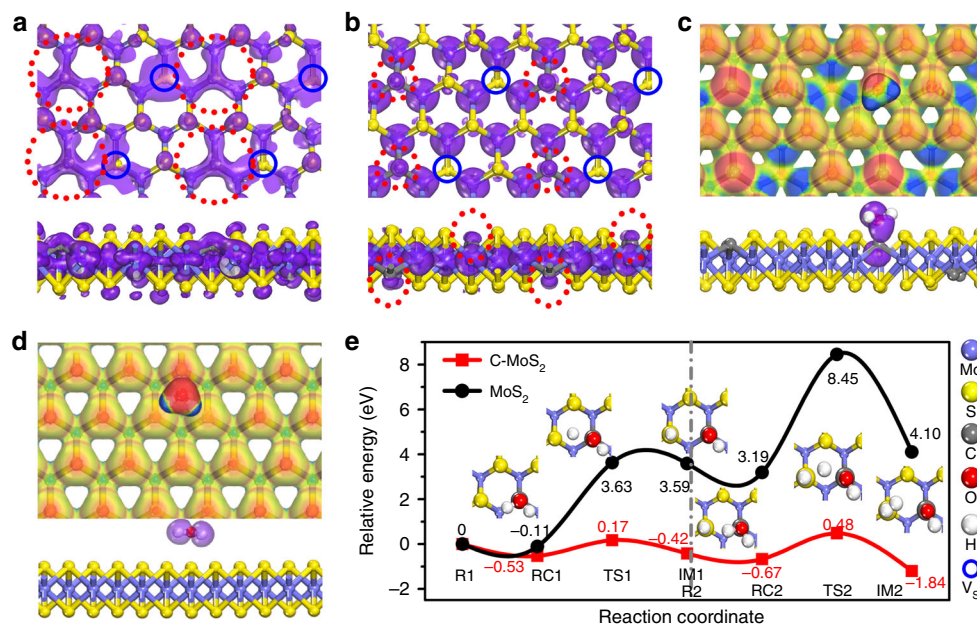


Fig. 5 The structural analysis and the catalytic pathway of C-MoS₂. The top-view and side-view sp² hybrid orbitals (highlighted by red dash circle) at the top of valence band (a) and the empty 2p orbitals (highlighted by red dash circle) perpendicular to the basal plane at the bottom of conduction band (b) of C-MoS₂. The top-view electrostatic potential of water adsorbed on the basal plane of C-MoS₂ (c) and MoS₂ (d) and the corresponding side-view bonding and non-bonding orbitals. e The relative energy diagram along the reaction coordinate, including the first (left panel) and second (right panel) water dissociation process on the basal plane of MoS₂ and C-MoS₂, respectively. R reactant, RC reactant complex, TS transition state, IM intermediate

(Supplementary Fig. 20) indicates that carbon doping can well increase the electrical conductivity of the MoS₂ and thus could benefit the electron transportation and enhance the catalytic activity. Although conductivity is important for electrocatalysis, we reasonably believe the exceptional alkaline HER activity of C-MoS₂ is mainly stemmed from the C-induced orbital tuning for water adsorption and dissociation, considering 1-T MoS₂ with better conductivity does not exhibit such exceptional activity⁴⁹. Moreover, the electrostatic potential mapping images (Fig. 5c and Supplementary Fig. 21) and the electron density difference slices (Supplementary Fig. 22) further reveal superior water adsorption on the basal plane of C-MoS₂, which is confirmed by the apparent charge transfer and the formation of remarkable chemical bonding orbital between water and C-MoS₂ (Fig. 5c), while no apparent orbital bonding or charge interaction occurs on MoS₂ (Fig. 5d). We also consider the MoS₂ model with only sulfur vacancies. Structural analysis indicates sulfur vacancies indeed do not have obvious effects on the orbital orientation tuning (Supplementary Fig. 23a). The corresponding water adsorption energy on the defected MoS₂ (MoS₂-Vs) is around -0.23 eV, which is only slightly higher than that on the MoS₂. Meanwhile, we also experimentally prepare MoS₂ with sulfur vacancies via a typical hydrogen treatment and study their electrochemical properties. The overall performance of the hydrogen treated MoS₂ is still far less than that of C-MoS₂ (Supplementary Fig. 23b), suggesting the sulfur vacancy may not be the main factor for the exceptional alkaline HER activity of the C-MoS₂. Taken together, all the structural information consistently suggest that carbon doping can effectively manipulate the orbital orientation and create more active sites on the basal plane of MoS₂ for water adsorption and activation.

Besides structural information, alkaline HER catalytic pathways on the basal plane of MoS₂ and C-MoS₂ are further studied. Figure 5e shows the relative energy profiles of water adsorption and dissociation on MoS₂ and C-MoS₂, respectively. As expected, the basal plane of MoS₂ is almost inert for alkaline HER catalysis,

with poor water adsorption and giant water dissociation energy barrier. Impressively, carbon doping enables the HER catalysis to proceed on a much lower potential energy surface. Specifically, C-MoS₂ owns more favorable adsorption energies (-0.53 eV for RC1 & -0.25 eV for RC2) and much lower transition state energy barrier (0.70 eV for TS1 & 1.15 eV for TS2). From the water adsorption/dissociation configurations on C-MoS₂ (Fig. 5e), H₂O is adsorbed on the C site, while the nearby S sites assist water dissociation by attracting the H in water molecule. In addition, we also performed the catalytic pathway of Mo₂C (001) (Supplementary Fig. 24). Obviously, the reaction on the Mo₂C proceeds on a potential energy surface with much higher energy barrier than that on C-MoS₂. Moreover, the generated hydrogen adsorbed intermediate (Sur-H) is so stable that the adsorbed hydrogen needs overcome 1.37 eV for H desorption from the carbon site of the surface, which could potentially impede the HER catalysis. The studies on the catalytic pathways clearly reveal carbon doping could intrinsically boost the water adsorption and dissociation kinetics and thus endow MoS₂ with exceptional alkaline catalysis by tuning the orbital orientations on the basal plane.

In summary, we have demonstrated carbon doping can intrinsically endow MoS₂ with exceptional alkaline HER catalytic capability by tuning the orbital orientation. In comparison with the inert alkaline HER activity of MoS₂, the prepared C-MoS₂ achieves an overpotential of 45 mV at 10 mA cm⁻², which is very close to the commercial Pt/C and also represents the best catalytic activity among the ever-reported MoS₂ for alkaline HER catalysis. XPS and XAS analysis reveal that the electronic and coordination structures of MoS₂ have been significantly changed after carbon doping. DFT studies further indicate that carbon-induced empty 2p orbitals perpendicular to the basal plane of MoS₂ enable energetically favorable water adsorption and dissociation, and thus promote the alkaline HER catalytic kinetics. The capability to intrinsically manipulate the catalytic activities by orbital modulation could offer a powerful platform to rationally design HER catalysts and beyond.

Methods

Reagents and chemicals. Ammonium molybdate ((NH₄)₆Mo₇O₂₄·4H₂O), Potassium hydroxide, Cetyltrimethyl ammonium bromide (CTAB), Thiourea and Sublimed sulfur were purchased from Shanghai Sinopharm Chemical Reagent Co., Ltd. CC was purchased from Shanghai Hesun Electric Co., Ltd.

Synthesis of Mo₂C. Typically, 3.708 g ammonium molybdate and 1.638 g CTAB were dissolved in 30 mL and 180 mL deionized water with ultrasonic assistance, respectively. Then, the two solutions were mixed homogeneously by magnetically stirring for 30 min, and further aged for another 24 h to obtain a uniform emulsion. A volume of 15 mL of the as-prepared emulsion was transferred into a 20 mL Teflon-lined stainless steel autoclave with the pretreated CC (CC, 2*3 cm², pretreated with nitric acid and deionized water, respectively) as the growth substrate. After keeping the autoclave at 200 °C for 20 h, the CC was taken out, cleaned by deionized water and dried at vacuum oven at 60 °C overnight. Finally, Mo₂C was obtained by annealing the prepared samples at 900 °C for 6 h in a home-built tube furnace system under argon atmosphere.

Synthesis of C-MoS₂ and MoS₂. C-MoS₂ and MoS₂ were prepared by a temperature-controlled sulfurization process. The as-prepared Mo₂C was sulfurized in a tube furnace system for 2 h with powdered sulfur as the sulfur source and argon as the carrier gas (flowing rate at 20 sccm). The sulfurization temperatures can be tuned from 500 to 900 °C. The optimized C-MoS₂ was achieved at 600 °C with a partial sulfurization, while MoS₂ was fabricated at 900 °C with a deep sulfurization. As comparison, a post-doping strategy was employed to dope carbon into MoS₂. The carbon doped MoS₂ by post-doping method (PC-MoS₂) was achieved by annealing MoS₂ at 750 °C for 0.5 h under acetylene flow. MoS₂ with minimum carbon interference was synthesized by sulfurizing ammonium molybdate with S as the sulfur source and argon as the carrier gas (flowing rate at 20 sccm) for 2.0 h under 900 °C²⁵.

Structural characterizations. XRD measurements were performed on a Philips X'Pert Pro Super diffractometer using Cu K α radiation ($\lambda = 1.54178 \text{ \AA}$). The field-emission scanning (FE-SEM) images were collected using a FEI Sirion-200 SEM, while TEM and HRTEM images were acquired at a JEOL-2010 TEM with an acceleration voltage of 200 kV. Raman spectra were recorded on a Renishaw RM 3000 Micro-Raman system. XPS were performed at the photoemission end-station (BL10B) in the National Synchrotron Radiation Laboratory (NSRL), Hefei. To avoid the carbon interference for the binding energy calibration, all the samples were sprayed with tiny amount of Au as an external standard and the obtained binding energies were calibrated using the Au 4f energy (Au 4f_{7/2}, binding energy of 84 eV). The XPS fitting was performed using the XPS PEAK41 software with Shirley background subtraction. The XPS database (NIST X-ray Photoelectron Spectroscopy Database, <https://srdata.nist.gov/xps/intro.aspx>) was used as a reference to assign the possible chemical states. During fitting, the peak intensity ratio and the full width at half maximum (FWHM) were well constrained in a reasonable range. XAS measurements were conducted at the beamline (BL14W1) of Shanghai National Synchrotron Radiation Facility (SSRF, China). The EXAFS data were disposed according to the standard procedures through the ATHENA module implemented in the IFEFFIT software packages⁵⁰. The quantitative curve-fittings were conducted for the Fourier-transformed k²-weighted $\chi(k)$ in the R-space with a Fourier transform k-space range of 3.1–11 \AA^{-1} by employing the module ARTEMIS 4 of IFEFFIT. The backscattering amplitude F(k) and phase shift $\Phi(k)$ were calculated by FEFF8.0 code. While the curve-fitting, all the amplitude reduction factor S₀² was set to the best-fit value of 0.85 determined from fitting the data of MoS₂. In order to fit the curves in the R-range of 1.1–3.4 \AA , we considered Mo–C, Mo–Mo and Mo–S paths as the central-peripheral. For each path, the structural parameters, like coordination number (N), interatomic distance (R), and edge-energy shift (ΔE_0) were opened to be varied. For the Mo–C, Mo–S, and Mo–Mo coordination, the common adjustable parameters of ΔE_0 and σ^2 were employed to reduce the number of free parameters.

Electrochemical measurements. All the electrochemical characterizations were performed in a three-electrode system on CHI 760E electrochemical workstation. The studied materials grown on CC were used as working electrodes, while Hg/HgO electrode and graphite rod were employed as the reference and counter electrodes, respectively. All the measurements were conducted in 1.0 M KOH electrolyte and the potentials vs. Hg/HgO were converted with respect to the reversible hydrogen electrode (RHE) using the equation $E \text{ (vs. RHE)} = E \text{ (vs. Hg/HgO)} + E^0 \text{ (Hg/HgO)} + 0.059 \text{ pH}$ in the 1.0 M KOH. LSV curves were collected with a scan rate of 5 mV s⁻¹ and the LSV curves shown in the manuscript were corrected by IR compensation ($E_{\text{IR-corrected}} = E_{\text{original}} - I \cdot R_s$). The chronoamperometry curve was performed for the durability test at the potential of -0.1 V vs. RHE. Electrochemical surface area (ECSA) was obtained by conducting cyclic voltammery (CV) in the range of 0.1–0.2 V vs. RHE with various scan rates from 10 to 50 mV s⁻¹. The current density differences ($\Delta j = j_a - j_c$) were plotted against scan rates, and the slopes can be used to derive C_{dl} and the ECSA. EIS measurements were carried out at the potential of -0.1 V (vs. RHE) in the frequency range of 100,000–0.001 Hz with a perturbation of 5 mV. TOF values were calculated using a previously reported method, in which the number of active sites was estimated as the amount of surface sites (including C, Mo, and S atoms)¹¹. The

Faradic efficiency of C-MoS₂ was evaluated in a H-type cell with an anion exchange membrane as the separator and 20 mL 1.0 M KOH as the electrolyte in each compartment, with a gas chromatography (HA GC-9560) for the hydrogen gas detection. The gas production was detected by the gas chromatography and the Faradic efficiency was calculated using the formula: Faradic efficiency = $2 F \times N_{\text{H}_2} / Q = 2 F \times N_{\text{H}_2} / (It)$, where F is the Faradic constant, I is the current, t is the running time and N_{H₂} is the amount of H₂ production.

Density functional theory calculation. All the DFT calculations were carried out using the CASTEP program in Material Studio package of Accelrys Inc⁵¹. The exchange-correlation functional was employed by the Perdew-Burke-Ernzerhof (PBE) of generalized gradient approximation (GGA) with the ultrasoft pseudopotentials (USP). The van der Waals interactions was considered by the DFT dispersion correction (DFT-D). The number of plane wave was determined by an energy cutoff of 450 eV. The Brillouin zone was sampled by a 2 × 2 × 1 k-points grid for the structure optimizations and double k-points meshes were employed for the density of states (DOS) calculations, respectively. A complete linear synchronous transitions (LST) and quadratic synchronous transitions (QST) approach was used for the transition state searching. The convergence tolerances were set to 2.0 × 10⁻⁶ eV per atom for energy, 0.002 \AA for maximum displacement, and 0.05 eV \AA^{-1} for maximum force. The surfaces were modeled by a periodic slab repeated in 6 × $\sqrt{2}$ × 2 $\sqrt{2}$ surface unit cell with a vacuum region of 13 \AA between the slabs along the z axis. The H₂O absorption energy was calculated using the following equation, $\Delta E_{\text{H}_2\text{O}} = E_{\text{surf-H}_2\text{O}} - E_{\text{surf}} - E_{\text{H}_2\text{O}}$, where E_{surf-H₂O} and E_{surf} are the total energies of the surface covered with and without H₂O molecule, E_{H₂O} is the energy of free H₂O molecule.

Data availability

The authors declare that the main data to support the finds of this study are available within the article and its Supplementary Information. Extra data are available from the corresponding author upon request

Received: 17 August 2018 Accepted: 28 February 2019

Published online: 14 March 2019

References

- Seh, Z. W. et al. Combining theory and experiment in electrocatalysis: Insights into materials design. *Science* **355**, 4998–5010 (2017).
- Roger, I., Shipman, M. A. & Symes, M. D. Earth-abundant catalysts for electrochemical and photoelectrochemical water splitting. *Nat. Rev. Chem.* **1**, 1–13 (2017).
- Stamenkovic, V. R., Stamenkovic, D. S., Lopes, P. P. & Markovic, N. M. Energy and fuels from electrochemical interfaces. *Nat. Mater.* **16**, 57–69 (2017).
- Zheng, Y., Jiao, Y., Vasileff, A. & Qiao, S. Z. The hydrogen evolution reaction in alkaline solution: from theory, single crystal models, to practical electrocatalysts. *Angew. Chem. Int. Ed.* **57**, 7568–7579 (2018).
- Gao, M. R., Chan, M. K. & Sun, Y. Edge-terminated molybdenum disulfide with a 9.4- \AA interlayer spacing for electrochemical hydrogen production. *Nat. Commun.* **6**, 7493 (2015).
- Wang, S. T. et al. Ultrafine Pt nanoclusters confined in a calixarene-based {Ni₂4} coordination cage for high-efficient hydrogen evolution reaction. *J. Am. Chem. Soc.* **138**, 16236–16239 (2016).
- Staszak-Jirkovsky, J. et al. Design of active and stable Co-Mo-Sx chalcogenides as pH-universal catalysts for the hydrogen evolution reaction. *Nat. Mater.* **15**, 197–203 (2016).
- Fang, Z. W. et al. Dual Tuning of Ni-Co-A (A = P, Se, O) Nanosheets by anion substitution and holey engineering for efficient hydrogen evolution. *J. Am. Chem. Soc.* **140**, 5241–5247 (2018).
- Zhu, C. R. et al. In situ grown epitaxial heterojunction exhibits high-performance electrocatalytic water splitting. *Adv. Mater.* **30**, 1705516 (2018).
- Li, J. Y. et al. Mechanistic insights on ternary Ni_{2-x}Co_xP for hydrogen evolution and their hybrids with graphene as highly efficient and robust catalysts for overall water splitting. *Adv. Funct. Mater.* **26**, 6785–6796 (2016).
- Wu, Y. S. et al. Electron density modulation of NiCo₂S₄ nanowires by nitrogen incorporation for highly efficient hydrogen evolution catalysis. *Nat. Commun.* **9**, 1425 (2018).
- Chen, Z. Y. et al. Tailoring the d-band centers enables Co₄N nanosheets to be highly active for hydrogen evolution catalysis. *Angew. Chem. Int. Ed.* **57**, 5076–5080 (2018).
- Kou, T. Y. et al. Theoretical and experimental insight into the effect of nitrogen doping on hydrogen evolution activity of Ni₃S₂ in alkaline medium. *Adv. Energy Mater.* **8**, 1703538 (2018).
- Tran, P. D. et al. Coordination polymer structure and revisited hydrogen evolution catalytic mechanism for amorphous molybdenum sulfide. *Nat. Mater.* **15**, 640–646 (2016).

15. Chen, P., Zhang, Z. W., Duan, X. D. & Duan, X. F. Chemical synthesis of two-dimensional atomic crystals, heterostructures and superlattices. *Chem. Soc. Rev.* **47**, 3129–3151 (2018).
16. Tsai, C. et al. Electrochemical generation of sulfur vacancies in the basal plane of MoS₂ for hydrogen evolution. *Nat. Commun.* **8**, 15113 (2017).
17. Kong, D. S. et al. Synthesis of MoS₂ and MoSe₂ films with vertically aligned layers. *Nano. Lett.* **13**, 1341–1347 (2013).
18. Li, Y. et al. MoS₂ nanoparticles grown on graphene: an advanced catalyst for the hydrogen evolution reaction. *J. Am. Chem. Soc.* **133**, 7296–7299 (2011).
19. Hu, J. et al. Nanohybridization of MoS₂ with layered double hydroxides efficiently synergizes the hydrogen evolution in alkaline media. *Joule* **1**, 383–393 (2017).
20. Xie, J. F. et al. Defect-rich MoS₂ ultrathin nanosheets with additional active edge sites for enhanced electrocatalytic hydrogen evolution. *Adv. Mater.* **25**, 5807–5813 (2013).
21. Yu, M. H. et al. Engineering thin MoS₂ nanosheets on TiN nanorods: advanced electrochemical capacitor electrode and hydrogen evolution electrocatalyst. *ACS Energy Lett.* **2**, 1862–1868 (2017).
22. Tao, L., Duan, X., Wang, C., Duan, X. & Wang, S. Plasma-engineered MoS₂ thin-film as an efficient electrocatalyst for hydrogen evolution reaction. *Chem. Commun.* **51**, 7470–7473 (2015).
23. Deng, S. J. et al. Phase modulation of (1T-2H)-MoS₂/TiC-C shell/core arrays via nitrogen doping for highly efficient hydrogen evolution reaction. *Adv. Mater.* **30**, 1802223 (2018). <https://doi.org/10.1002/adma.1802223>.
24. Deng, S. J. et al. Directional construction of vertical nitrogen-doped 1T-2H MoS₂/graphene shell/core nanoflake arrays for efficient hydrogen evolution reaction. *Adv. Mater.* **29**, 170048 (2017).
25. Li, G. Q. et al. All the catalytic active sites of MoS₂ for hydrogen evolution. *J. Am. Chem. Soc.* **138**, 16632–16638 (2016).
26. Yin, Y. et al. Contributions of phase, sulfur vacancies, and edges to the hydrogen evolution reaction catalytic activity of porous molybdenum disulfide nanosheets. *J. Am. Chem. Soc.* **138**, 7965–7972 (2016).
27. Jaramillo, T. F. et al. Identification of active edge sites for electrochemical H₂ evolution from MoS₂ nanocatalysts. *Science* **317**, 100–102 (2007).
28. Hinnemann, B. et al. Biomimetic hydrogen evolution MoS₂ nanoparticles as catalyst for hydrogen evolution. *J. Am. Chem. Soc.* **127**, 5308–5309 (2005).
29. Kibsgaard, J., Chen, Z. B., Reinecke, B. N. & Jaramillo, T. F. Engineering the surface structure of MoS₂ to preferentially expose active edge sites for electrocatalysis. *Nat. Mater.* **11**, 963–969 (2012).
30. Voiry, D. et al. The role of electronic coupling between substrate and 2D MoS₂ nanosheets in electrocatalytic production of hydrogen. *Nat. Mater.* **15**, 1003–1009 (2016).
31. Geng, X. M. et al. Three-dimensional structures of MoS₂ nanosheets with ultrahigh hydrogen evolution reaction in water reduction. *Adv. Funct. Mater.* **24**, 6123–6129 (2014).
32. Pu, Z. H. et al. 3D macroporous MoS₂ thin film: in situ hydrothermal preparation and application as a highly active hydrogen evolution electrocatalyst at all pH values. *Electrochim. Acta* **168**, 133–138 (2015).
33. Zhang, B. et al. Interface engineering: The Ni(OH)₂/MoS₂ heterostructure for highly efficient alkaline hydrogen evolution. *Nano Energy* **37**, 74–80 (2017).
34. Zhang, J. et al. Interface Engineering of MoS₂/Ni₃S₂ heterostructures for highly enhanced electrochemical overall-water-splitting activity. *Angew. Chem. Int. Ed.* **55**, 6702–6707 (2016).
35. Zhao, G. Q. et al. CoSe₂/MoSe₂ Heterostructures with enriched water adsorption/dissociation sites towards enhanced alkaline hydrogen evolution reaction. *Chem. Eur. J.* **24**, 11158–11165 (2018).
36. Xiong, Q. Z. et al. Cobalt covalent doping in MoS₂ to induce bifunctionality of overall water splitting. *Adv. Mater.* **30**, 1801450 (2018).
37. Sun, T. et al. Engineering the electronic Structure of MoS₂ nanorods by N and Mn dopants for ultra-efficient hydrogen production. *ACS Catal.* **8**, 7585–7592 (2018).
38. Fan, M. H. et al. Growth of molybdenum carbide micro-islands on carbon cloth toward binder-free cathodes for efficient hydrogen evolution reaction. *J. Mater. Chem. A* **3**, 16320–16326 (2015).
39. Huang, Y. et al. Mo₃C Nanoparticles dispersed on hierarchical carbon microflowers for efficient electrocatalytic hydrogen evolution. *ACS Nano* **10**, 11337–11343 (2016).
40. Shi, Y. et al. Energy level engineering of MoS₂ by transition-metal doping for accelerating hydrogen evolution reaction. *J. Am. Chem. Soc.* **139**, 15479–15485 (2017).
41. Li, G. Q. et al. Activating MoS₂ for pH-universal hydrogen evolution catalysis. *J. Am. Chem. Soc.* **139**, 16194–16200 (2017).
42. Deng, J. et al. Multiscale structural and electronic control of molybdenum disulfide foam for highly efficient hydrogen production. *Nat. Commun.* **8**, 14430 (2017).
43. Xie, J. F. et al. Controllable disorder engineering in oxygen-incorporated MoS₂ ultrathin nanosheets for efficient hydrogen evolution. *J. Am. Chem. Soc.* **135**, 17881–17888 (2013).
44. Lassalle-Kaiser, B. et al. Evidence from in situ X-ray absorption spectroscopy for the involvement of terminal disulfide in the reduction of protons by an amorphous molybdenum sulfide electrocatalyst. *J. Am. Chem. Soc.* **137**, 314–321 (2015).
45. Shi, Z. P. et al. Phosphorus-Mo₂C@carbon nanowires toward efficient electrochemical hydrogen evolution: composition, structural and electronic regulation. *Energy Environ. Sci.* **10**, 1262–1271 (2017).
46. Zhang, J. et al. Engineering water dissociation sites in MoS₂ nanosheets for accelerated electrocatalytic hydrogen production. *Energy Environ. Sci.* **9**, 2789–2793 (2016).
47. Xing, Z. C., Yang, X. R., Asiri, A. M. & Sun, X. P. Three-dimensional structures of MoS₂@Ni core/shell nanosheets array toward synergetic electrocatalytic water splitting. *ACS Appl. Mater. Interfaces* **8**, 14521–14526 (2016).
48. Amiin, I. S. et al. Multifunctional Mo-N/C@MoS₂ electrocatalysts for HER, OER, ORR, and Zn-Air batteries. *Adv. Funct. Mater.* **27**, 1702300 (2017).
49. Yan, Y., Xia, B. Y., Xu, Z. C. & Wang, X. Recent development of molybdenum sulfides as advanced electrocatalysts for hydrogen evolution reaction. *ACS Catal.* **4**, 1693–1705 (2014).
50. Ankudinov, A. L., Ravel, B., Rehr, J. J. & Conradson, S. D. Real-space multiple-scattering calculation and interpretation of X-ray-absorption near-edge structure. *Phys. Rev. B* **58**, 7565–7576 (1998).
51. Clark, S. J. et al. First principles methods using CASTEP. *Z. fuer Krist.* **220**, 567–570 (2005).

Acknowledgements

We thank the financial support of the National Key Research and Development Program of China (2017YFA0206703), Natural Science Fund of China (No. 21771169, 11722543, 11505187), the Fundamental Research Funds for the Central Universities (WK2060190074, WK2060190081, and WK231000066), USTC start-up funding, and Recruitment Program of Global Expert. We also acknowledge the beamline BL10B at National Synchrotron Radiation Laboratory, and the Beamline BL14W1 at Shanghai Synchrotron Radiation Facility for XPS and XAFS characterizations. The numerical calculations in this paper have been done on the supercomputing system in the Supercomputing Center of University of Science and Technology of China.

Author contributions

G.W. and Y.Q. designed and supervised the project. Y.Z. and S.N. conducted the project and contributed equally to this work. J.Y., Y.W., X.Z. and J.Zhu conducted XPS and XAS measurements. J.C., Y.X., Y.L. and J.Z. performed SEM and TEM characterization. X.L. and S.N. provided the DFT calculation. G.W., Y.Z. and X.L. wrote and revised the manuscript, and all the authors discussed the results and commented on the manuscript.

Additional information

Supplementary Information accompanies this paper at <https://doi.org/10.1038/s41467-019-09210-0>.

Competing interests: the authors declare no competing interests.

Reprints and permission information is available online at <http://npj.nature.com/reprintsandpermissions/>

Journal peer review information: *Nature Communications* thanks the anonymous reviewer(s) for their contribution to the peer review of this work. Peer reviewer reports are available.

Publisher's note: Springer Nature remains neutral with regard to jurisdictional claims in published maps and institutional affiliations.



Open Access This article is licensed under a Creative Commons Attribution 4.0 International License, which permits use, sharing, adaptation, distribution and reproduction in any medium or format, as long as you give appropriate credit to the original author(s) and the source, provide a link to the Creative Commons license, and indicate if changes were made. The images or other third party material in this article are included in the article's Creative Commons license, unless indicated otherwise in a credit line to the material. If material is not included in the article's Creative Commons license and your intended use is not permitted by statutory regulation or exceeds the permitted use, you will need to obtain permission directly from the copyright holder. To view a copy of this license, visit <http://creativecommons.org/licenses/by/4.0/>.

© The Author(s) 2019